Diffuse Fluorescence Tomography Analysis of B-Scan Mode Geometry

Dax Kepshire, Summer Gibbs, Scott Davis, Hamid Dehghani, Keith D. Paulsen and Brian W. Pogue

Thayer School of Engineering, Dartmouth College, Hanover NH 03755
(Email: Dax.Kepshire@dartmouth.edu, Tel:(603) 646-2685, Fax:(603) 646-3856)

Astract: A fluorescence diffuse optical tomography system capable of producing B-scan-type images of localized fluorescence regions is presented. The B-Scan mode is analogous to ultrasound where the excitation and remission signals are delivered from the tissue surface.

OCIS codes:

1. Introduction

Diffuse tomography for fluorescence imaging has been successfully demonstrated in several important applications, most notably in small animal transmittance tomography[1-3], and with some pilot studies in larger animals in remission mode[4]. There has been no clear evidence that remission mode, or so called B-scan mode (more common in Ultrasound technology) is going to provide a useful imaging geometry. In this paper, the remission mode or B-scan mode geometry is evaluated both computationally and experimentally using a raster scanned light source and a CCD detector. In remission mode, an A-scan would compromise a single excitation point where the emissive field is then collected. A B-scan mode would then be where the light source was scanned across a line of points on the surface, and the remitted field is captured at each successive point. In this study, this latter 2-D mode of depth tomography imaging is examined, with a focus on what information it could provide, given an optimized image reconstruction algorithm. In particular in this abstract, the effect of spatially varying depth regularization is examined[5]. The results have implications for utilization of the reflectance geometry for depth tomography in many areas of research or medicine, such as small animal imaging of localized regions, or even subsurface imaging in humans with specific contrast agents.

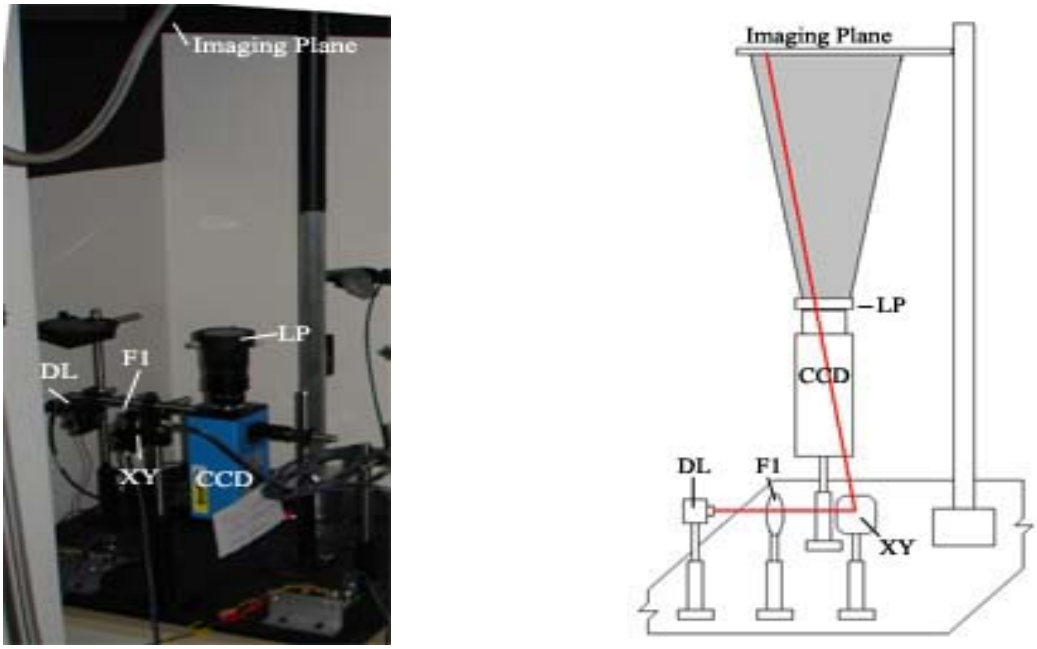

(a) **(b)**

Figure 1: The experimental setup is comprised of an excitation light source (LD), two orthogonal galvanometers (XY) for raster scanning the source position, a long-pass filter (LP) for filtering out the excitation light, a filter for attenuating the excitation light (F1), and a CCD (CCD) camera for detection. The picture of the experimental setup is shown in Figure 1 (a) and a schematic is illustrated in Figure 1 (b).

2. Methods

2.1 Experimental Setup

The non-contact fluorescence diffuse optical tomography (DOT) imaging system is depicted in Figure 1(a) and is schematically shown in Figure 1(b). The optimal remission imaging geometry was determined to be 16 sources and 32 detectors (480 measurements) by performing sensitivity and singular-value decomposition analysis of the fluorescence Jacobian for various source/detector combinations [1,2]. A 4x4 pixel binning scheme is employed, allowing one binned pixel to serve as a detector; for this work a source spacing of 2.5 mm and a detector spacing of 1.25 mm was used. A 635 nm collimated diode laser (Model CPS196, Thor Labs) and two orthogonal galvanometers (Model 6220, Cambridge Technology) are used to raster scan the source position. The amplitude of both the excitation signal and the remitted Protoporphyrin IX (PpIX) fluorescence signal, separated by a 650 nm long-pass filter, is then detected using a cooled CCD camera (Sensicam QE, Cooke Corporation). Intensity images are acquired for all source positions along the surface of the tissue and used to generate a calibrated data set by:

$$\phi^{i}_{calibrated} = \left[\left(\phi^{i}_{m\_hetero} - \phi^{i}_{m\_homo}\right)\times 10^{OD}\right]\times SF\,; \qquad SF = \frac{\Phi^{i}_{x}}{\left(\phi^{i}_{x}\right)\times 10^{OD}}$$

where the subscripts *x* and *m* denote excitation and emission respectively; ϕ_{m_homo} and ϕ_{m_hetero} fluorescence intensity before and after administration of a fluorescent agent; ϕ_x is the absorption at excitation; OD represents the attenuation magnitude of the source; and Φ_x is absorption data generated by solving the forward problem on a model with the same optical properties. The calibrated fluorescence intensity data is then used as amplitude boundary data in the reconstruction technique described in section *2.2 Image Reconstruction* to recover fluorescence yield.

2.2 Image Reconstruction

The transport of fluorescence in a turbid media can be described by the coupled diffusion equations:

$$\nabla\cdot D_x(\vec{r})\nabla\phi_x(\vec{r},\omega) - \left[\mu_{ax}(\vec{r}) + i\omega/c\right]\phi_x(\vec{r},\omega) = -q_0(\vec{r},\omega) \tag{1}$$

$$\nabla\cdot D_m(\vec{r})\nabla\cdot\phi_m(\vec{r},\omega) - \left[\mu_{am}(\vec{r}) + i\omega/c\right]\phi_m(\vec{r},\omega) = -\phi_x(\vec{r},\omega)\eta\mu_{af}(\vec{r})\frac{1-i\omega\tau(\vec{r})}{1-[\omega\tau(\vec{r})]^2} \tag{2}$$

where the subscripts *x* and *m* denote excitation and emission wavelengths respectively; $q_0(\vec{r},\omega)$ is an isotropic excitation source term; ω is the modulation frequency at excitation; ϕ_x and ϕ_m are the excitation and emission fields; μ_{ax} and μ_{am} represent the absorption coefficients; μ_{af} is the absorption due to fluorophore; D_x and D_m are the diffusion coefficients; τ is the lifetime; η is the fluorophore's quantum efficiency. Using a Newton-Raphson algorithm and Robin-type (type III) boundary conditions the spatial distribution of fluorescent yield is recovered by solving the inverse problem for the coupled diffusion equations iteratively on a finite-element model. Spatially variant regularization was implemented to improve image contrast and resolution deep into the model [3].

2.3 Simulations

Simulations were performed using FluoroFAST, an in-house software package (S. Davis & H. Dehghani, Dartmouth College). Simulated boundary data (1% noise added) was generated on a 2000 node mesh using the optical properties μ_a = 0.01mm^{-1} and μ_s' =0.1 mm^{-1}, μ_{af} = 0.005 mm^{-1} and for a 5mm anomaly between 0mm and 10mm in 2.5mm increments. The data was then used to reconstruct images for fluorescence yield using the reconstruction technique described previously. Images of the reconstructed fluorescence yield for anomalies with 5:1 contrast at locations 0, 2.5, 5, and 7.5mm are depicted in Figure 2 (a)-(d) respectively; for reference, the true positions and values of $\eta\mu_{af}$ are shown in Figure 2 (e)-(f). This procedure was repeated for μ_{af} values of 0.002 mm^{-1}, 0.003 mm^{-1}, and 0.004 mm^{-1}.

3. Results

From Figure 2 it is obvious that the quantitative accuracy of the recovered fluorescence yield and size of the anomaly (FWHM) depreciate with distance from the boundary. However, it was found that the position of the anomaly can accurately be recovered by determining the centroid of the maximum cross section in fluorescence

yield intensity. These calculations were performed on the reconstructed images in Figure 1 and the results of all simulations described in *Section 2.3*; these results are summarized in Figure 3 below.

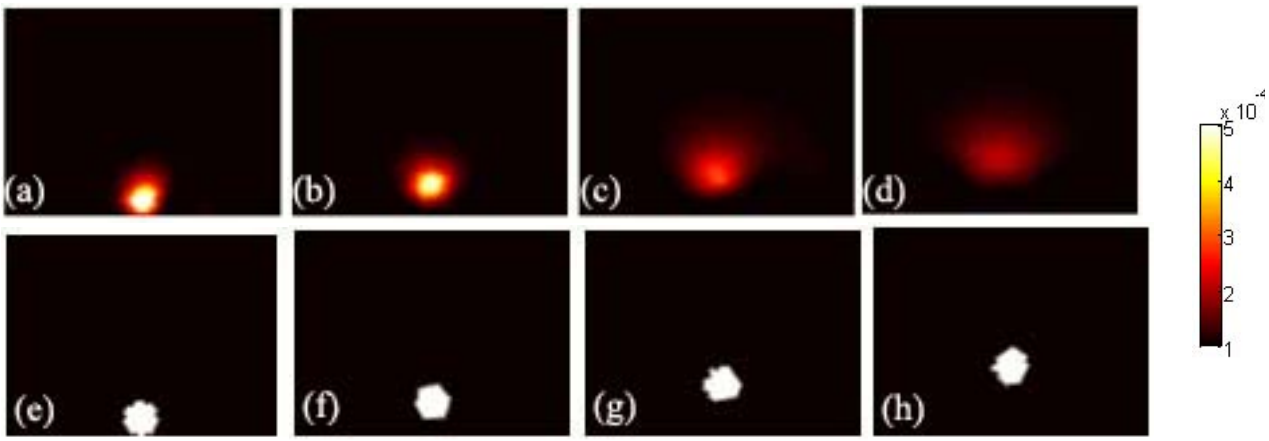

Figure 2: Reconstructed images of fluorescence yield for a 5mm anomaly with 5:1 contract at positions 0mm (a) and (e), 2.5mm (b) and (f), 5mm (c) and (g), and 7.5mm (d) and (h).

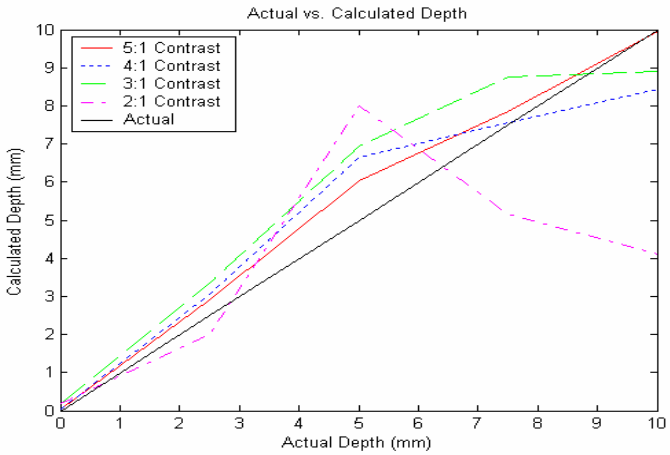

Figure 3: Centroid locations for reconstructed images of 5mm anomaly with 5:1, 4:1, 3:1, and 2:1 contrasts at various depths.

4. Discussion

It has been shown that location of inclusions can accurately be predicted for contrasts above of 3:1. This may prove useful in applications such as sub-surface imaging of the brain where there is a low background endogenous fluorescence and contrasts above 3:1 are possible. Research is ongoing to improve the accuracy of not only the centroid location, but also the fluorescence yield concentration and FWHM of the recovered anomaly.

5. Acknowledgements

This work was sponsored by NIH grants RO1CA109558 and U54CA105480.

6. References

1. Ntziachristos, V., Tung, C. H., Bremer, C., Weissleder, R., "Fluorescence molecular tomography resolves protease activity *in vivo*" Nat Med. 2002 Jul;8(7):757-60 (2002).
2. Xu H, Dehghani H, Pogue BW, Springett R, Paulsen KD, Dunn JF., "Near-infrared imaging in the small animal brain: optimization of fiber positions," Journal of Biomedical Optics 8(1), 102-110 (2003).
3. J. P. Culver, V. Ntziachristos, M. J. Holboke, and A. G. Yodh, ''Optimization of optode arrangements for diffuse optical tomography: a singular-value analysis,'' *Opt. Lett.* 26(10), 701–703 (2001).
4. Godavarty A, Sevick-Muraca EM, Eppstein MJ. "Three-dimensional fluorescence lifetime tomography." Med Phys. 2005 Apr;32(4):992-1000.
5. Pogue, B. W., McBride, T., Prewitt, J., Osterberg U. L., Paulsen, K. D., "Spatially variant regularization improves diffuse optical tomography," Applied Optics 38(13), 2950-2961 (1999).